# Theoretical study of magnetism and Mössbauer hyperfine interactions in ordered FeNi and disordered fcc Fe-rich Fe–Ni alloys

Diana Guenzburger and Joice Terra

*Centro Brasileiro de Pesquisas Físicas, rua Xavier Sigaud 150, 22290-180 Rio de Janeiro, RJ, Brazil*

Electronic structure spin-polarized calculations with the discrete variational method in density functional theory were performed for 79-atoms embedded clusters modeling the ferromagnetic (FM) ordered layered compound FeNi (tetrataenite), as well as disordered Fe-rich fcc Fe–Ni alloys containing ~15% Ni in an antiferromagnetic (AFM) configuration. These phases of Fe–Ni may be obtained by synthetic means, and are also present in meteorites. Spin magnetic moments and spin density maps were obtained from the calculations. The $^{57}$Fe Mössbauer hyperfine parameters isomer shift, quadrupole shift and magnetic hyperfine fields were calculated with the self-consistent charge and spin densities obtained. It was found that for FM ordered FeNi the electric-field gradient is positive; this result, together with the measured positive value of the quadrupole shift, proves that the direction of magnetization is perpendicular to the Fe–Ni layers. For the Fe-rich disordered Fe–Ni alloys with AFM configuration, it was found that the lower values of the isomer shift relative to tetrataenite can only be explained by a lattice contraction.

PACS number(s): 75.50.−y

## I. INTRODUCTION

Fe–Ni alloys have been the subject of great scientific interest for many decades, due to their structural, mechanical, and magnetic properties. The complex phase diagram shows the existence of both $\gamma$ (fcc) and $\alpha$ (bcc) phases;[1] the fcc phase has complex magnetic behavior, and is known to exist in different magnetic states,[2] similar to pure fcc Fe.[3–5] Furthermore, at a certain Fe–Ni composition range (~30–40 at. % Ni) the fcc disordered alloys present vanishing thermal expansion coefficients; this property is known as INVAR and is important in metallurgical applications.[2]

The lower temperature portion ($T < 400\ °C$) of the Fe–Ni phase diagram has a complex structure that includes a paramagnetic low-Ni disordered fcc phase, as well as the ordered compounds FeNi (tetrataenite) and $Ni_3Fe$.[1] However, due to the fcc→bcc martensitic transformation, the Fe-rich paramagnetic disordered phase (<30 at% Ni) can only be obtained by less-conventional methods, in the form of fine particles,[6] thin films prepared with molecular-beam epitaxy,[7] or by mechanical alloying.[8–12]

On the other hand, iron meteorites are composed of Fe–Ni alloys with only small amounts of other elements.[13] They have played an important role in the study of the Fe–Ni phase diagram at low temperatures, due to the fact that they have cooled at a rate of about 1 °C for $10^6$ years, and this allowed thermodynamic equilibrium to take place. In the $\gamma$ phase of meteoritical Fe–Ni, called taenite, may be found disordered $Fe_{(1-x)}Ni_x$ alloys of various compositions.[14] The ordered phase FeNi 50–50 (tetrataenite), which cannot be obtained in the laboratory by simple annealing due to the extremely low diffusion rate below the critical ordering temperature $T = 320\ °C$, is an important component of iron meteorites.[14–17] Ordered FeNi can also be obtained by irradiation of the disordered 50-50 alloy with neutrons or electrons,[18,19] which accelerates diffusion.

Mössbauer spectroscopy of $^{57}$Fe has been an important tool in identifying and investigating these Fe–Ni phases, in meteorites,[13,14,17,20–22] as well as in artificially prepared samples.[7–11,19] Information such as magnetic state, order-disorder ratios, chemical environment, etc., may be extracted from the spectra. The Mössbauer hyperfine parameters isomer shift ($\delta$), quadrupole shift ($\varepsilon$), and magnetic hyperfine field ($H_F$) give fundamental information on the different phases and the local environment of Fe.

In this work we focus on two well-characterized metastable forms of Fe–Ni which are present in meteorites, and may also be obtained by laboratory means: the ordered 50-50 FeNi compound which has the AuCu layered structure (tetrataenite), and the disordered paramagnetic $\gamma$ phase with low Ni content. The latter has been identified as forming a fine intergrowth with tetrataenite in meteorites,[23] and it was proposed as a new mineral. Since the single Mössbauer peak of the paramagnetic fcc phase was shown to exhibit a broadening at low temperatures in the Santa Catharina meteorite,[24] this phase was considered to be an antiferromagnetic (AFM) Fe–Ni alloy with a paramagnetic→AFM transition temperature $T_N \sim 25$ K. The paramagnetic phase was accordingly named antitaenite, and the intergrowth tetrataenite/antitaenite has since been identified in other meteorites.[25] The AFM synthetic analogue of antitaenite has been recently identified in mechanically alloyed $Fe_{100-x}Ni_x$ ($x=21$, 24, 27 at %),[11] employing Mössbauer spectroscopy at low temperatures, and estimating $T_N \sim 40$ K for $x=24$ at. %, which is somewhat lower than $T_N \sim 65$ K of low-moment AFM fcc Fe.[3]

Fe–Ni disordered alloys have been the subject of numerous experimental and theoretical investigations over the years, specially those in the INVAR region of composition, due to their technological importance. Electronic structure calculations within density functional theory (DFT) and the local spin-density approximation (LSDA) have been reported.[26–38] The coherent potential approximation (CPA), in which each atom is considered to be in the average potential of the disordered alloy, has been employed together with the Korringa–Kohn–Rostocker (CPA-KKR) band-structure

method[26–31,38] as well as the linear muffin-tin orbitals band-structure scheme.[34,35] Although most of the work reported has been for ferromagnetic (FM) alloys, a disordered local moment model was applied to Fe–Ni alloys in the INVAR concentration, to account for the possibility of antiparallel spin alignment.[31–33] Calculations allowing for noncollinear spin alignments have also been reported.[36,37] Magnetic hyperfine fields have been obtained with the CPA-KKR method for $Fe_xNi_{(1-x)}$ in the FM state.[27,38]

Here we adopted a different approach, and performed first-principles real-space DFT electronic structure calculations within the LSD approximation for 79 atoms embedded clusters representing the solids. The numerical self-consistent spin-polarized discrete variational method (DVM)[39,40] was employed. This methodology is adequate to describe localized properties of metals and alloys, such as local magnetic moments and Mössbauer hyperfine parameters; at the same time, the size of the clusters is already sufficient to assure that most of the long-range interactions are properly included. The DVM method was applied successfully to investigate the magnetic and hyperfine properties of the related systems fcc Fe[41] and fcc Fe particles in Cu.[42] Other applications of DVM to metallic systems include transition metal impurities in metallic hosts,[43–45] Co particles in a Cu host[46] and overlayers of fcc Fe on Cu.[47]

In this paper we report the results of embedded-cluster calculations performed with the DV method for two components of the Fe–Ni phase diagram: the ordered FM compound FeNi formed by alternating layers of Fe and Ni, and a disordered fcc Fe–Ni alloy with ~15% Ni. For the former, the electric-field gradient and Mössbauer quadrupole shift on Fe were obtained; the spin magnetic moments on Fe and Ni were calculated, as well as the contact and dipolar components of the magnetic hyperfine field on Fe. Maps of electronic charge distribution were derived, to explain the origin of the electric-field gradient. For the latter, an AFM configuration was considered, and calculations were performed for two different lattice parameters and two different local Fe–Ni distributions, in order to assess the effect of Ni neighbors and interatomic distances on the local properties of Fe in this alloy. Spin magnetic moments, hyperfine fields, and Mössbauer isomer shifts on Fe were obtained. Calculations were also performed for FM and AFM $\gamma$-Fe for comparison.

This paper is organized as follows: in Sec. II we describe concisely the theoretical method, in Sec. III we present the results for ordered FeNi, in Sec. IV we present the results for a disordered fcc FeNi alloy, and in Sec. IV we summarize our conclusions.

## II. THEORETICAL METHOD

First-principles spin-polarized electronic structure calculations were performed for 79-atoms clusters embedded in the external potential of the solids, employing the numerical discrete variational method (DVM) in density functional theory and the local spin-density approximation. The DV method has been described in the literature.[39,40] The Kohn–Sham equations of DFT are solved self-consistently for the cluster in a three-dimensional grid of points, where the po-

tential is a functional of the electron charge density $\rho_\sigma(\mathbf{r})$ of each spin $\sigma$. In the spin-polarized scheme, the density pertaining to each spin may be different, driven by the exchange interaction. The total density $\rho(\mathbf{r})$ is given by $[\rho\uparrow(\mathbf{r}) + \rho\downarrow(\mathbf{r})]$, where the arrows stand for $m_s = +(-)1/2$, and the spin density $\rho_s(\mathbf{r})$ is defined as $[\rho\uparrow(\mathbf{r}) - \rho\downarrow(\mathbf{r})]$. In the embedding scheme, the densities of both spins of ~1000 atoms neighbors to the cluster in the lattice sites of the external solid were also included. These are obtained self-consistently by DFT-LSDA numerical atomic calculations. The embedding provides a realistic external potential that stabilizes the cluster, and it is optimized by considering at the external atomic sites atomic densities obtained for atoms with the same configuration (electronic occupation of the orbitals) as in the cluster, as defined by a Mulliken population analysis[40] after an initial set of iterations.

The size of the cluster is such as to guarantee that local properties, such as local spin magnetic moments and hyperfine parameters, when obtained at the central atom of the cluster, are within ~5% of convergence. Previous cluster calculations for various types of solids[41–49] showed that the values of local properties at the central atom in general are acceptably converged with 3–4 shells of neighbors.

The density of each spin is obtained by a sum over the one-particle functions $\phi_\sigma^i$ of the cluster

$$\rho_\sigma(\mathbf{r}) = \sum_i n_\sigma^i |\phi_\sigma^i(\mathbf{r})|^2 \tag{1}$$

where $n_\sigma^i$ is the occupation number. Each $\phi_\sigma^i$ is defined as a linear expansion over numerical atomic orbitals (linear combination of atomic orbitals), whose coefficients are determined by solving the secular equations of the DV method in a three-dimensional grid of points. Group theory is invoked to obtain symmetry orbitals, in order to break down the secular matrix and render the calculations tractable. The atomic orbitals of the basis were obtained self-consistently with numerical DFT-LSDA calculations for the atoms. Since the orbitals are central field solutions, they depend only on one variable $r$; this numerical problem is relatively simple, and one may say that the numerical solutions for the orbitals are obtained exactly, since they are completely converged in the number of points of the one-dimensional grid. The basis obtained in this way is thus more compact and better than any analytical basis (such as a set of Gaussians), since the latter are constructed to reproduce the former, and this will never be completely accomplished in practice. Furthermore, in the DV method the basis is optimized in the following manner: after an initial set of iterations for the cluster, a Mulliken population analysis is performed to obtain the occupations of the atomic orbitals in the atoms of the cluster. These occupations are then used to define atomic configurations in the atomic calculations performed to generate an improved basis. This procedure may be repeated a few times to obtain a basis adapted to the cluster.

The local exchange-correlation potential employed was that of Vosko, Wilk, and Nusair.[50] A model density is employed to construct the cluster potential, which is an overlapping expansion in multipoles centered at the cluster nuclei.[51] This expansion is fitted to the "real" density by least-squares

minimization. We have used only terms with $l=0$, which is adequate for compact structures of metals. In general, and unless otherwise stated, the local properties are calculated for the central atom of the cluster, since it is less affected by the truncation of the cluster, and its environment best represents that of the solid. The orbitals included in the variational space were $3d$, $4s$, and $4p$ for Fe and Ni. The inner (core) orbitals were considered "frozen" after the first iteration, when they are explicitly orthogonalized to the orbitals of the valence. Atomic charges and spin magnetic moments were obtained by integrating the electronic charge density $\rho(\mathbf{r})$ and spin density $\rho_s(\mathbf{r})$, respectively, inside the Wigner–Seitz volume of the atom.

Once the self-consistent density is obtained, the hyperfine parameters may be calculated. The Mössbauer isomer shift $\delta$ is given by[52]

$$\delta = \alpha[\rho_A(0) - \rho_S(0)], \tag{2}$$

where $\alpha$ includes nuclear terms and a correction for relativistic effects, and the term in brackets is the difference in the electronic density at the nucleus of absorber $A$ and source $S$. In a nonrelativistic theory, only $s$ electrons penetrate the nucleus. Since the core was frozen in the calculations, only the valence spin density was obtained from the cluster calculations. The core contribution ($1s$, $2s$, and $3s$) to $\rho(0)$ was obtained separately by atomic numerical DFT-LSDA calculations for free Fe with the configuration (occupation number of the atomic orbitals) that it had in the cluster, as defined by a Mulliken population analysis.[40] In practice, only the Fe $3s$ contribution to $\rho(0)$ shows any difference from one environment to another, the $1s$ and $2s$ being too contracted to experience chemical effects. Here we have used the value $\alpha = -0.23$ for $^{57}$Fe.[53]

In magnetic solids, the quadrupole shift $\varepsilon$ of the magnetically split nuclear levels of the $I=3/2$ excited state of the 14.4 keV Mössbauer transition of $^{57}$Fe is defined as[54]

$$\varepsilon = 1/4 \; eV_{zz}Q(3\cos^2\theta - 1)/2, \tag{3}$$

where $\theta$ is the angle between the direction of the magnetization and the principal axis of the field gradient $V_{zz}$, e is the charge of the proton (e$=1$ in atomic units) and $Q$ is the quadrupole moment of the nucleus in the excited state. The principal component of the electric field gradient in axial field is calculated as

$$V_{zz} = - e \int \rho(\mathbf{r})(3z^2 - r^2)/r^5 d\mathbf{r} + \Sigma_q Z_q^{\text{eff}}(3z_q^2 - r_q^2)/r_q^5, \tag{4}$$

where the first term is the electronic contribution of the cluster and the second term is the contribution of the nuclei of the cluster atoms around the Fe site of atomic number $Z$, with effective charges $Z_q^{\text{eff}} = Z - n_c$ ($n_c=$ number of core electrons).

The magnetic hyperfine interactions may be decomposed in three contributions:[55]

$$H_F = H_c + H_D + H_L. \tag{5}$$

The first term is the contact or Fermi contribution $H_c$ given by
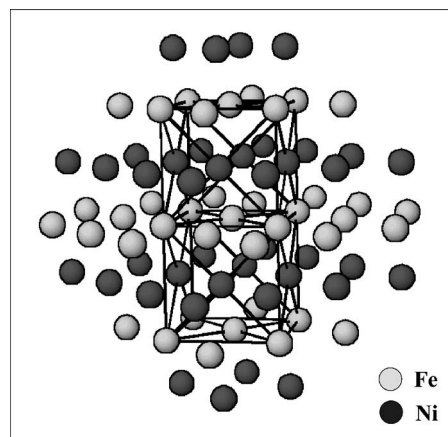


FIG. 1. Representation of the 79 atoms cluster modeling the intermetallic layered compound FeNi (tetrataenite). The lines are drawn to show the underlying fcc structure, which is slightly distorted ($c \neq a, b$).

$$H_c = 8\pi/3 \; \mu_B \rho_s(0), \tag{6}$$

where $\mu_B$ is the Bohr magneton and $\rho_s(0)$ is the spin density at the nucleus. In a nonrelativistic approach, only $s$ electrons contribute to $\rho_s(0)$. As for the isomer shifts, since the core was frozen in the calculations, only the valence spin density was obtained from the cluster calculations. The core contribution ($1s$, $2s$, and $3s$) to $\rho_s(0)$ was obtained separately by atomic numerical DFT-LSDA calculations for free Fe with the configuration (occupation number of the atomic orbitals) that it had in the cluster, as defined by a Mulliken population analysis.[40]

The dipolar contribution $H_D$ arises from an anisotropy of the spin density around the nucleus; the principal component of the dipolar tensor $H_D$ in axial symmetry is given by

$$H_D^{zz} = \mu_B \int \rho_s(\mathbf{r})(3z^2 - r^2)/r^5 d\mathbf{r} \tag{7}$$

The dipolar tensor is traceless, and thus by symmetry we have

$$H_D^{xx} = H_D^{yy} = - 1/2 \; H_D^{zz}. \tag{8}$$

Within a nonrelativistic or scalar relativistic approach the orbital angular momentum is completely quenched in a solid, and thus the orbital field $H_L=0$. The quenching of the orbital angular momentum is incomplete if spin-orbit coupling is taken into account, as in a relativistic treatment, giving rise to a nonvanishing $H_L$. A relativistic calculation for FeNi alloys gave values of $H_L$ for Fe of the order of 20 kG.[27]

### III. ORDERED FeNi (TETRATAENITE)

In Fig. 1 is depicted the 79-atoms cluster representing tetrataenite. This intermetallic compound is ferromagnetic (FM) and has an AuCu layered structure, with alternating layers of Fe and Ni. The lattice is a slightly distorted fcc, with a small elongation along the $c$ axis ($c/a=1.0036$) which confers it tetragonal symmetry.[15] Our cluster is centered on
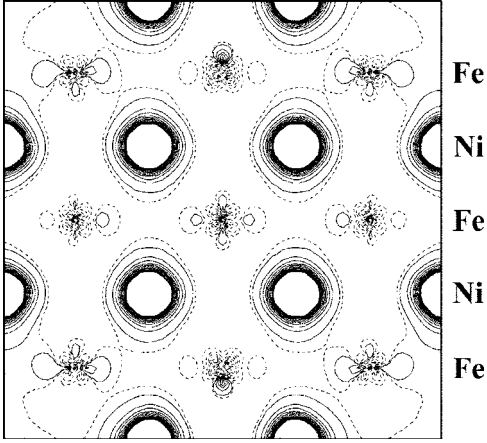
FIG. 2. Map of the electronic charge difference $D(\mathbf{r})$ $=[\rho(\mathbf{r})(\text{FeNi}) - \rho(\mathbf{r})(\text{Fe})]$ on a plane perpendicular to the Fe and Ni layers of tetrataenite, and containing the nuclei of Fe and Ni atoms. Contours are from 0.001 to 0.1 $a_0^{-3}$, and from $-0.001$ to $-0.1$ $a_0^{-3}$, with intervals of 0.00825 $a_0^{-3}$. Solid lines are positive values, dotted lines are negative values.

an Fe atom, where the Fe local properties are calculated. In this structure each Fe atom is surrounded by four Fe and eight Ni nearest neighbors. For comparison, we have also done calculations for an analogous cluster of FM fcc Fe, with the same lattice parameters as FeNi.

Integration of the electronic charge inside the Wigner–Seitz cell of each atom shows a small accumulation of negative charge on the Ni sites, in accordance with the slightly higher electronegativity of the latter with respect to Fe. This is more clearly seen on a map of the difference density $D(\mathbf{r})$, defined as

$$D(\mathbf{r}) = [\rho(\mathbf{r})(\text{FeNi}) - \rho(\mathbf{r})(\text{Fe})] \qquad (9)$$

which may be viewed in Fig. 2 It may be seen from this figure that, as compared to a lattice of pure Fe with atoms at exactly the same lattice sites as FeNi, the Ni sites show a considerable accumulation of electronic charge ($D(\mathbf{r})>0$), consistent with the surplus of two electrons in this atom relative to Fe; however, the depletion of electronic charge clearly visible at the Fe sites in FeNi ($D(\mathbf{r})<0$) is evidence of the Fe→Ni charge transfer.

Integration of the spin density $\rho_s(\mathbf{r})$ inside the Wigner–Seitz cell of the central Fe atom of the cluster representing FeNi gives a spin magnetic moment of $2.6\mu_B$; the same in-

tegration on a Ni nearest neighbor gives $0.6\mu_B$. For the cluster representing fcc Fe, a ferromagnetic solution was also obtained with a moment on the Fe of $2.2\mu_B$. The fact that Fe in FeNi has a larger moment than in fcc Fe at the same lattice constants may be explained by a smaller Fe–Ni hybridization in tetrataenite, due to the more contracted 3$d$ orbitals of Ni. A larger hybridization tends to decrease the magnetic moment on an atom by filling the minority spin 3$d$ orbitals, which are more extended.

The tetragonal layered structure creates an anisotropic charge distribution around each Fe atom, and thus an electric-field gradient is produced. The latter is reflected in the quadrupole shift $\varepsilon$ given by Eq. (3), measured by Mössbauer spectroscopy. Although the sign of $\varepsilon$ was measured,[19] the angle $\theta$ between the principal axis of the field gradient $V_{zz}$ and the direction of magnetization [see Eq. (3)] was not determined experimentally, and thus the sign of $V_{zz}$ could not be obtained from the Mössbauer experiments.

The value of $V_{zz}$, calculated according to Eq. (4), is $+0.443$ $a_0^{-3}$. It is seen that the sign is positive; this result, coupled with the measured positive sign of $\varepsilon$, indicates unambiguosly that $\theta=0$, that is, the axis of $V_{zz}$, which coincides with the tetragonal symmetry axis, is parallel to the internal magnetic field. This result confirms an earlier prediction, from a calculation done for a considerably smaller cluster (19 atoms),[56] that the direction of magnetization is perpendicular to the lamellae.

In Table I is given the calculated value of $\varepsilon$, together with the experimental value obtained for synthetic ordered FeNi, as well as for samples from meteorites. The higher values of $\varepsilon$ measured for the synthetic samples, obtained by irradiation of the disordered alloy with neutrons or electrons,[19] must be considered as pertaining to pure tetrataenite. The fact that lower values of $\varepsilon$ are found in some meteorites is assumed to be evidence of some disorder produced by reheating or shock, that occurred some time during the meteorite's history.[13]

The origin of the electric-field gradient may be inferred from the calculations as being the electronic charge anisotropy, with accumulation of electron charge in the Ni layers and depletion of the Fe layers, as seen in Fig. 2. The small tetragonal distortion of the lattice only contributes with a small fraction of the total $\varepsilon$. This was confirmed by a calculation for the cluster representing FM fcc Fe, with the same lattice parameters of tetragonal ordered FeNi: the value of $\varepsilon$ obtained was only $+0.05$ mm/s.

Our calculated value of $\varepsilon$ is still somewhat higher than the highest values measured. This could be ascribed to the ne-

TABLE I. Hyperfine parameters of Fe in tetrataenite.

| Lattice constants[a] (Å) | $\varepsilon^{\text{b}}$(mm/s) | $\varepsilon$(exp.)(mm/s) | $H_c$(kOe) | $H_D$(kOe) | $H_F$(kOe) | $H_F$(exp.)[d](kOe) |
|---|---|---|---|---|---|---|
| $a=3.576$ | $+0.35$ | $+0.13$ to $+0.24^{\text{c}}$ | $-255$ | $H_D^{zz}=+14$ | $-241(\perp)$ | $-288(\perp)$ |
| $c=3.589$ | | $+0.23^{\text{d}}$ | | $H_D^{xx}=-7$ | $-262(\parallel)$ | $-327(\parallel)$ |
| | | | | $H_D^{yy}=-7$ | | |

[a]From Ref. 15.
[b]Value of $Q$ in Eq. (3) taken as 0.16 b (from Ref. 58).
[c]From Ref. 20 (in samples from different meteorites).
[d]From Ref. 19 (in monocrystals of ordered FeNi obtained by neutron irradiation).

glect of the contribution from the core orbitals polarization, especially the $3p$, although this contribution was found to be almost negligible in band-structure calculations for hcp metals.[57] Another factor leading to this discrepancy could be uncertainties in the value $Q = 0.16$ b[58] employed here.

In Table I are also given the calculated values of the contact hyperfine field $H_c$, the components of the electronic dipolar field $H_D$ and the total hyperfine field $H_F$. The values of the experimental hyperfine field perpendicular ($\perp$) and parallel ($\parallel$) to the layers are also given in Table I. The contact field is large and negative, indicating the dominance of the core contribution. It is seen that the components of the dipolar field are far from negligible, and account for most of the difference between parallel and perpendicular total fields measured in monocrystals of tetrataenite.[19] This result is somewhat analogous to the case of multilayers of Fe in Cu, which may be considered a somewhat similar system to the present layered compound.[59] Inclusion of the orbital hyperfine field could increase this anisotropy further.[59] The magnitudes of the calculated $H_F$ are smaller than the experimental values; this is due to a well-known effect of the local density approximation, which systematically underestimates the core spin polarization, and thus gives $H_c$ values for Fe of smaller magnitudes. A satisfactory solution to this limitation of the LSDA has not yet been reached.

The dipolar field originates from the anisotropy of the spin density around an Fe atom between the (001) plane perpendicular to the lamellae and the horizontal Fe plane, as may be seen in Figs. 3(a) and 3(b). In these figures may also be visualized the spin polarization of the conduction electrons in the interstitial region, with AFM coupling relative to the more contracted $3d$ spin densities.

It is interesting to notice that, although the calculation for FM Fe at the same lattice constants gives a smaller value for the magnetic moment in Fe than in ordered FeNi (2.2 $\mu_B$, as compared to 2.6 $\mu_B$), $H_c$ has a larger magnitude in pure Fe ($-271$ kOe, as compared to $-255$ kOe in FeNi). This is due to the different signs of the valence contribution, which is negative in pure Fe and thus adds to the negative core contribution, and positive in FeNi, which added to the negative core contribution gives a net value of $H_c$ of smaller magnitude. Earlier calculations for FM fcc Fe at different lattice constants have consistently found negative values for the valence contribution to $H_c$.[41]

### IV. Fe–Ni DISORDERED fcc ALLOY (∼15% Ni)

As discussed in the Introduction, a paramagnetic disordered fcc $Fe_{100-x}Ni_x$ phase with low Ni content has been detected in artificially prepared samples, as well as in meteorites. Recent Mössbauer spectroscopy measurements at low temperatures on mechanically obtained alloys[11] have identified the magnetic state of this phase as low-moment AFM, with a Néel temperature of ∼40 K for $x = 24$. This phase was also detected in many meteorites, where it was named antitaenite and proposed as a new mineral; in the case of the Santa Catharina meteorite, it is believed to have ∼15% Ni content.[23,60] The AFM transition of the paramagnetic phase at low temperatures has also been observed in the Santa Catharina meteorite.[61]
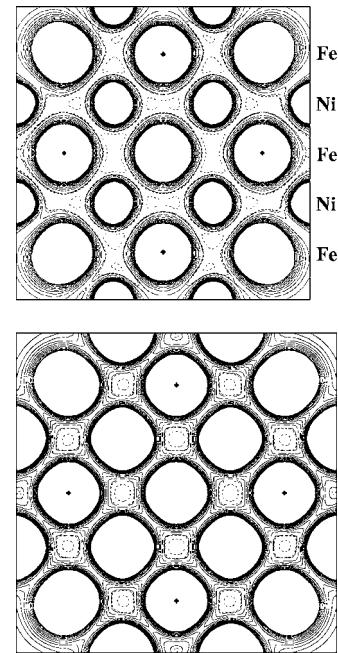


FIG. 3. (a) Map of the spin density $\rho_s(\mathbf{r}) = [\rho\uparrow(\mathbf{r}) - \rho\downarrow(\mathbf{r})]$ on a plane perpendicular to the Fe and Ni layers of tetrataenite, and containing the nuclei of Fe and Ni atoms. Contours are from 0.0001 to 0.01 $a_0^{-3}$, and from $-0.0001$ to $-0.01$ $a_0^{-3}$, with intervals of 0.000 825 $a_0^{-3}$. Solid lines are positive values, dotted lines are negative values. (b) Map of the spin density $\rho_s(\mathbf{r}) = [\rho\uparrow(\mathbf{r}) - \rho\downarrow(\mathbf{r})]$ of tetrataenite on the Fe plane containing the nucleus of the central Fe of the cluster. Contour specifications as in Fig. 3(a). Solid lines are positive values, dotted lines are negative values.

To study the magnetic and hyperfine properties of this alloy, we constructed two different clusters to model a disordered fcc Fe–Ni alloy with ∼15% Ni; these are shown in Figs. 4(a) and 4(b). The clusters were chosen as to reflect two different environments for the central Fe atom, one in which it has no Ni nearest neighbors [configuration A, Fig. 4(a)] and another in which it has four Ni nearest neighbors in skewed positions [configuration B, Fig. 4(b)]. The positions of all 12 Ni atoms in the clusters were chosen as to be as evenly distributed as possible, while at the same time maintaining some point symmetry ($D_{2d}$), without which the calculations would not be viable. Since no statistical method was employed to estimate the probability of occurrence of such configurations, they were considered solely to assess *local* electronic and magnetic effects on Fe in such environments.

At this range of low Ni concentration, it is reasonable to expect the AFM alloy to have similar properties to AFM $\gamma$-Fe. It is known by theory[62,63] and experiment[3–5] that fcc Fe has a high-moment FM state at larger lattice constants, and an AFM low-moment state at smaller lattice constants. The lattice constant found at the energy minimum for AFM $\gamma$-Fe by band structure calculations with the linear augmented plane wave method was 6.38 a.u. (3.38 Å);[62] however, this number may be somewhat small due to the local density approximation employed. Calculations performed later for AFM $\gamma$-Fe with the modified augmented plane wave method with gradient corrections to the LSDA predicted a lattice
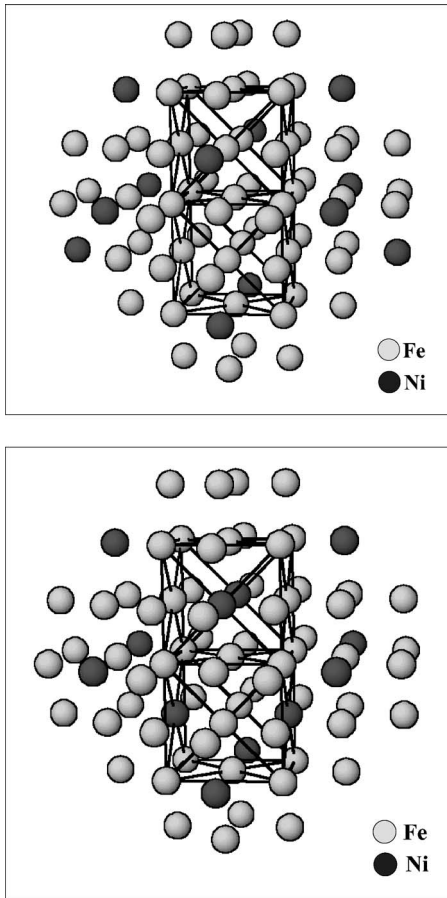
FIG. 4. (a). Representation of the 79 atoms cluster modeling configuration A of the Fe–Ni disordered alloy with ~15% Ni. Lines are drawn to show the fcc structure. In configuration A the central Fe atom has no Ni nearest neighbors. (b) Representation of the 79 atoms cluster modeling configuration B of the Fe–Ni disordered alloy with ~15% Ni. Lines are drawn to show the fcc structure. In configuration B the central Fe atom has four Ni nearest neighbors.

constant for the AFM state equal to 3.54 Å.[63] Therefore, we chose to perform our calculations for the 15% disordered AFM Fe–Ni models at two different lattice constants for each configuration A and B: 3.39 and 3.48 Å, both smaller than the lattice parameters of tetrataenite (seen in Table I). Since we did not perform total energy calculations to obtain structural parameters for the Fe–Ni alloy, we will be looking at trends of the magnetic and hyperfine properties with lattice constant variation.

The AFM configuration initially considered to start the self-consistent field (SCF) iterations was constituted of alternating planes of spin-up and spin-down moments along the (001) axis. However, during the self-consistent procedure, the initial layered AFM structure is preserved only for the Fe atoms; the Ni atoms tend to flip their spins in order to attain a maximum of FM-coupling bonds with their Fe nearest neighbors. This occurs in all cases, for lattice parameters 3.39 and 3.48 Å, as well as for both configurations A and B. The final converged spin density maps of configuration A at lattice parameters 3.39 and 3.48 Å may be seen in Figs. 5(a) and 5(b), respectively; and of configuration B at 3.39 and
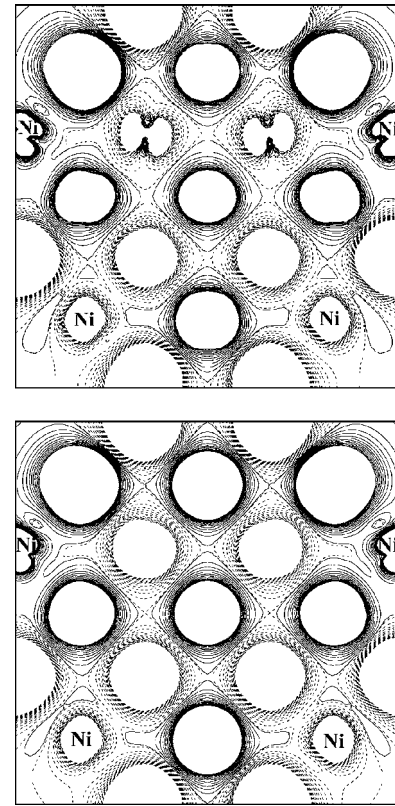


FIG. 5. (a) Map of the spin density $\rho_s(\mathbf{r}) = [\rho\uparrow(\mathbf{r}) - \rho\downarrow(\mathbf{r})]$ of configuration A of the Fe–Ni alloy with ~15% Ni, for lattice constant 3.39 Å, on a plane containing the (001) axis and containing the nuclei of Fe and Ni atoms. Contour specifications as in Fig. 3(a). Atoms not specified in the figure are Fe atoms. Solid lines are positive values, dotted lines are negative values. (b) Same caption as Fig. 5(a), but for lattice constant 3.48 Å.

3.48 Å, in Figs. 6(a) and 6(b), respectively. In these maps it may be observed that the Ni atoms have changed the sign of the spin that they had initially in a layer, in order to maximize the number of FM bonds with their Fe nearest neighbors. This is an indication that the Fe–Ni FM exchange coupling is energetically more favorable than AFM in these alloys. Thus one may expect that no simple AFM spin configuration is present in these alloys, as is stable in fcc Fe.[62] However, where Fe atoms exist with no Ni atoms as first neighbors, as is the case of the central Fe atom in configuration A [Figs. 5(a) and 5(b)], a local AFM alignment is stable. One must also keep in mind the possibility of a spiral spin structure in these fcc Fe-rich Fe–Ni alloys, as is known to be stable in pure fcc Fe.[63]

In Table II are given the calculated local properties spin magnetic moment, hyperfine field $H_F$ and isomer shift $\delta$ of Fe in fcc Fe$_{(1-x)}$Ni$_x$($x \cong 15\%$). For comparison, we have also performed calculations for an analogous cluster of AFM fcc Fe, at lattice constant 3.39 Å. This cluster was also constructed with alternating layers of spin-up and spin-down Fe moments; however, in this case, as had been seen earlier,[41,42] this alternating spin configuration is preserved during convergence of the SCF iterations.

In Table II it is seen that the Fe spin magnetic moments are smaller at the smaller lattice constant; this is expected
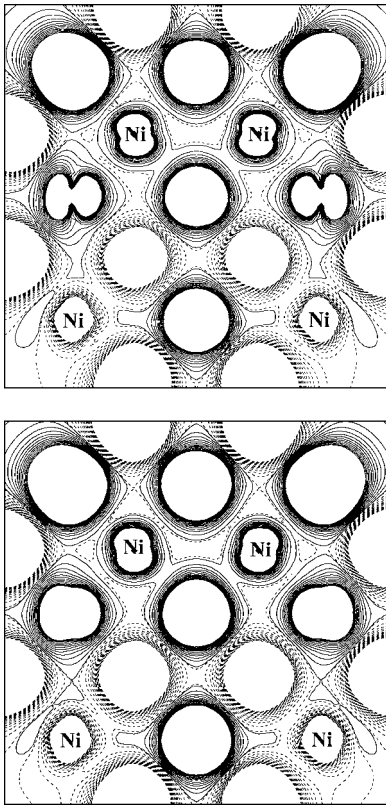
FIG. 6. (a) Map of the spin density $\rho_s(\mathbf{r})=[\rho\uparrow(\mathbf{r})-\rho\downarrow(\mathbf{r})]$ of configuration B of the Fe–Ni alloy with $\sim 15\%$ Ni, for lattice constant 3.39 Å, on a plane containing the (001) axis and containing the nuclei of Fe and Ni atoms. Contour specifications as in Fig. 3(a). Atoms not specified in the figure are Fe atoms. Solid lines are positive values, dotted lines are negative values. (b) Same caption as Fig. 6(a), but for lattice constant 3.48 Å.

since lattice compression tends to fill preferably the minority-spin $3d$ orbitals, which are more extended. Comparing with the calculation for pure $\gamma$-Fe at 3.39 Å, it is seen that the presence of Ni in the alloy enhances the magnetic moments on Fe, and more so for configuration B, where the central Fe atom on which we focus has four Ni nearest neighbors. This is due to the Fe$\rightarrow$Ni charge transfer, which depletes preferably the more extended $3d(\downarrow)$ orbital of Fe. The values of the hyperfine field $H_F$ are of small magnitudes, as expected from the small magnetic moments.

The last column of Table II gives the theoretical values of the isomer shifts $\delta$ for the Fe–Ni disordered alloys, calcu-

lated according to Eq. (2). The values of $\delta$ given are relative to the calculated value for the FeNi ordered compound (tetrataenite), i.e., the value for the latter has been shifted to $\delta=0$. It may be seen that all the calculated values of $\delta$ of the disordered alloys are lower than the value of tetrataenite; since $\alpha$ in Eq. (2) is negative, this means that the electron density at the Fe nucleus $\rho(0)$ is higher in the 15% fcc Fe–Ni alloys than in tetrataenite. This trend is in accordance with the experimental measurements of $\delta$ in low-Ni content Fe$_{(1-x)}$Ni$_x$ in synthetic samples[8,11] as well as in the "paramagnetic phase"[20,21,64] of meteoritic samples. The measured values of $[\delta(\text{paramagnetic phase})-\delta(\text{tetrataenite})]$ in non-shocked meteorites vary from $-0.9$ to $-0.13$ mm/s.[20,21,64] In fact, the values of $\delta$ of the low-moment low-Ni disordered fcc Fe–Ni alloys not only are lower than $\delta$ of the ordered FeNi (tetrataenite), but also of high-moment high-Ni disordered fcc Fe–Ni alloys. A compilation of values of $\delta$ for all these cases, after correction for the second-order Doppler shift, evidenced that the lower values of $\delta$ are a unique feature of the low-Ni disordered AFM fcc Fe–Ni alloys, and this fact was taken as proof of their distinct electronic structure.[60]

Observation of Table II shows that our calculated values are within the range of the experimental $\delta$ values, for lattice constant 3.48 Å. It may be seen also that the smaller lattice constant gives lower values of $\delta$ for both configurations A and B. The effect of Ni nearest neighbors is to increase the values of $\delta$, as may be noticed by comparing configuration B with configuration A at the same lattice constant. However, the effect of Ni neighbors is secondary to the effect of lattice compression; this may be confirmed further by comparing with the calculated $\delta$ of $\gamma$-Fe at lattice constant 3.39 Å, which is similar to $\delta$ of the alloy in configurations A and B, at this same lattice constant. Therefore, the present results for the isomer shift suggest that the main reason for the lower values of $\delta$ in the low-Ni AFM fcc Fe–Ni alloys is a lattice contraction relative to ordered FeNi or to the high-moment FM high-Ni alloys. This lattice contraction would be analogous to that of the low-moment AFM state of fcc Fe, relative to the high-moment FM. A decrease of the lattice parameter increases $\rho(0)$ by contraction of the valence wave functions towards the nucleus; this was seen in the noticeable effect of pressure upon the isomer shift of $\alpha$-Fe,[65] which decreases dramatically with increased pressure. In contrast, the isomer shift of an $^{57}$Fe impurity in Ni, relative to $\alpha$-Fe, is very small $(0.02$ mm/s),[66] which is evidence that the chemical effects of the host are small. The isomer shift of an Fe impurity in Ni, when corrected for volume effects, has a similar value.[67]

TABLE II. Local properties of Fe in AFM fcc Fe$_{(1-x)}$Ni$_x$ ($x\cong 0.15$) and AFM $\gamma$-Fe.

| | Config. | Lattice constant (Å) | Magnetic moment ($\mu_B$) | $H_F{}^a$(kOe) | $\delta^b$(mm/s) |
|---|---|---|---|---|---|
| Fe$_{(1-x)}$Ni$_x$ | A | 3.39 | 0.61 | −30 | −0.20 |
| | | 3.48 | 1.17 | −56 | −0.12 |
| Fe$_{(1-x)}$Ni$_x$ | B | 3.39 | 1.04 | −78 | −0.16 |
| | | 3.48 | 1.58 | −113 | −0.08 |
| $\gamma$-Fe | --- | 3.39 | 0.24 | −35 | −0.22 |

$^a$Contact contribution only.
$^b$Relative to ordered FeNi 50-50 (tetrataenite), for which the isomer shift was shifted to $\delta=0$.

## V. CONCLUSIONS

Self-consistent spin-polarized electronic structure calculations with the DV method were performed for 79-atoms embedded clusters modeling the ordered FM layered compound FeNi (tetrataenite), and the disordered AFM fcc alloy $Fe_{(1-x)}Ni_x$ with $x \cong 0.15$ in two different configurations of the Ni neighbors, and two different lattice parameters. Calculations were also performed for clusters representing FM and AFM $\gamma$-Fe for comparison.

In tetrataenite the spin magnetic moments on Fe are larger than in fcc Fe at the same lattice parameters (2.6 $\mu_B$, as compared to 2.2 $\mu_B$). Electron density maps show that there is an electronic charge transfer from the layers containing Fe atoms, to the layers containing Ni; this creates a charge anisotropy which originates the electric-field gradient on Fe. The calculated electric-field gradient at the Fe nucleus is positive; this result, together with the positive sign measured for the quadrupole shift, confirms an earlier prediction that the direction of magnetization is perpendicular to the lamellae, and coincides with that of $V_{zz}$. The electronic dipolar hyperfine field is noticeably large, due to the anisotropy of the spin density around the Fe atoms, as seen from spin-density maps, and explains largely the experimental anisotropy of the total hyperfine field. The magnitudes of the total hyperfine fields on Fe are approximately 20% smaller than experiment, which may be ascribed to the insufficient core polarization resulting from the LSDA.

The paramagnetic Fe-rich fcc Fe–Ni phase which may be obtained synthetically and is also detected in meteorites, and which is AFM at very low temperatures, was modeled by two clusters with different configurations containing $\sim 15\%$ Ni: one in which the central Fe has no Ni nearest neighbors, and another in which it has four Ni nearest neighbors. Two lattice parameters were considered in each case, both smaller than in ordered FeNi. An AFM spin configuration was initially assumed, consisting of alternating spin-up and spin-down layers; however, during the self-consistent iterations, the spin magnetic moments on the Ni atoms are seen to change sign, in order to maximize the number of FM-coupling bonds with its Fe nearest neighbors. The magnetic moments on Fe in the Fe–Ni alloy are enhanced relative to AFM $\gamma$-Fe at the same lattice constant. It is interesting to notice that, although our AFM model is restricted to alternating spin-up and spin-down layers, calculations for an alloy of INVAR composition ($Fe_{0.35}Ni_{0.65}$) with the locally self-consistent multiple scattering method, which allows for noncollinearity of the moments, also predict local collinear AFM alignment for Fe, when it is completely surrounded by other Fe atoms.[37] Therefore, our calculations for an alloy of lower Ni content also reveal that Fe clusters are responsible for the coexistence of antiferromagnetism with ferromagnetism in Fe–Ni alloys, which has been observed experimentally in $Fe_xNi_{(1-x)}$ INVAR alloys at low temperatures.[68,69]

It is concluded from the calculations that only a contraction of the lattice, relative to tetrataenite and to Ni-rich FM disordered fcc Fe–Ni alloys, can explain the significantly lower values of the isomer shift in the AFM alloys, in analogy to the lattice contraction of low-moment AFM $\gamma$-Fe relative to high-moment FM. In fact, the values of $\delta$ relative to bcc Fe in AFM $\gamma$-Fe (−0.088 mm/s) are indeed lower than in FM $\gamma$-Fe (+0.11 mm/s−+0.15 mm/s).[4] However, the values of the equilibrium lattice constants in the Fe–Ni alloys investigated here were not determined with the present calculations.

[1] W. D. Hopfe and J. I. Goldstein, Meteorit. Planet. Sci. **36**, 135 (2001).

[2] E. F. Wassermann, in *Ferromagnetic Materials*, edited by H. J. Buschow and E. P. Wohlfarth (Elsevier, Amsterdam, 1990), Vol. 5.

[3] W. A. A. Macedo and W. Keune, Phys. Rev. Lett. **61**, 475 (1988).

[4] R. D. Ellerbrock, A. Fuest, A. Schatz, W. Keune, and R. A. Brand, Phys. Rev. Lett. **74**, 3053 (1995), and references therein.

[5] D. J. Keavney, D. F. Storm, J. W. Freeland, I. L. Grigorov and J. C. Walker, Phys. Rev. Lett. **74**, 4531 (1995).

[6] H. Asano, J. Phys. Soc. Jpn. **27**, 542 (1969).

[7] J. W. Freeland, I. L. Grigorov, and J. C. Walker, Phys. Rev. B **57**, 80 (1998).

[8] R. Scorzelli, Hyperfine Interact. **110**, 143 (1997).

[9] Y. V. Baldokhin, V. V. Tcherdyntsev, S. D. Kaloshkin, G. A. Kochetov, and Y. A. Pustov, J. Magn. Magn. Mater. **203**, 313 (1999).

[10] S. D. Kaloshkin, V. V. Tcherdyntsev, Y. V. Baldokhin, I. A. Tomilin, and E. V. Shelekov, J. Non-Cryst. Solids **287**, 329 (2001).

[11] Y. A. Abdu, T. Ericsson, and H. Annersten, J. Magn. Magn. Mater. **280**, 395 (2004).

[12] Y. A. Abdu, H. Annersten, T. Ericsson, and P. Norblad, J. Magn. Magn. Mater. **280**, 243 (2004).

[13] R Scorzelli, Hyperfine Interact. **66**, 249 (1991).

[14] J. F. Albertsen, J. M. Knudsen, N. O. Roy-Poulsen, and L. Vistisen, Phys. Scr. **22**, 171 (1980).

[15] J. F. Albertsen, Phys. Scr. **23**, 301 (1981).

[16] J. F. Albertsen, G. B. Jensen, and J. M. Knudsen, Nature (London) **273**, 453 (1978).

[17] J. Danon, R. Scorzelli, I. Souza Azevedo, W. Curvello, J. F. Albersen, and J. M. Knudsen, Nature (London) **277**, 283 (1979).

[18] L. Neel, J. Pauleve, R. Pauthenet, J. Laugier, and D. Dautreppe, J. Appl. Phys. **35**, 873 (1964).

[19] Y. Gros and J. Pauleve, J. Phys. (France) **31**, 459 (1970).

[20] J. Danon, R. B. Scorzelli, I. Souza Azevedo, and M. Christophe-Michel-Levy, Nature (London) **281**, 469 (1979).

[21] R. B. Scorzelli and J. Danon, Phys. Scr. **32**, 143 (1985).

[22] J. Danon, R. B. Scorzelli, I. Souza Azevedo, and K. Imakuma, Phys. Scr. **21**, 223 (1980).

[23] D. G. Rancourt and R. B. Scorzelli, J. Magn. Magn. Mater. **150**, 30 (1995).

[24] E. De Grave, R. E. Vandenberghe, P. M. A. De Bakker, A. van Alboom, R. Vochten, and R. van Tassel, Hyperfine Interact. **70**, 1009 (1992).

[25] J. I. Goldstein, R. J. Reisner, D. G. Rancourt, K. Lagarec, and R. B. Scorzelli, Meteorit. Planet. Sci. **33S**, A59 (1998); R. B. Scorzelli and I. Souza Azevedo, *ibid.* **33S**, A128 (1998); R. B. Scorzelli, D. G. Rancourt, A. Bustamante Dominguez, G. Poupeau, C. Canut de Bon, and M. E. Cisternas, *ibid.* **32S**, A117 (1997).

[26] M. Schröter, H. Ebert, H. Akai, P. Entel, E. Hoffmann and G. G. Reddy, Phys. Rev. B **52**, 188 (1995).

[27] M. Battocletti and H. Ebert, Phys. Rev. B **64**, 094417 (2001).

[28] V. Crisan, P. Entel, H. Ebert, H. Akai, D. D. Johnson, and J. B. Staunton, Phys. Rev. B **66**, 014416 (2002).

[29] D. D. Johnson, F. J. Pinski, and J. B. Staunton, J. Appl. Phys. **61**, 3715 (1987).

[30] M. Schröter, H. Ebert, H. Akai, P. Entel, E. Hoffmann, and G. G. Reddy, Phys. Rev. B **52**, 188 (1995).

[31] H. Akai and P. H. Dederichs, Phys. Rev. B **47**, 8739 (1993).

[32] D. D. Johnson, F. J. Pinski, J. B. Staunton, B. L. Györffy, and G. M. Stocks, in *Physical Metallurgy of Controlled Expansion INVAR-Type Alloys* edited by K. C. Russell and D. F. Smith, (Minerals, Metals and Materials Society, Warrendale, PA, 1990), pp. 3–24.

[33] D. D. Johnson and W. A. Shelton, in *The INVAR effect: A centennial symposium*, edited by J. Wittenauer (Minerals, Metals and Materials Society, Warrendale, PA, 1997), pp. 63–74.

[34] I. A. Abrikosov, O. Eriksson, P. Söderlind, H. L. Skriver, and B. Johansson, Phys. Rev. B **51**, 1058 (1995).

[35] K. Lagarec, D. G. Rancourt, S. K. Bose, B. Sanyal, and R. A. Dunlap, J. Magn. Magn. Mater. **236**, 107 (2001).

[36] M. van Schilfgaarde, I. A. Abrikosov, and B. Johansson, Nature (London) **400**, 46 (1999).

[37] Y. Wang, G. M. Stocks, D. M. C. Nicholson, W. A. Shelton, V. P. Antropov, and B. N. Harmon, J. Appl. Phys. **81**, 3873 (1997).

[38] H. Ebert, H. Winter, B. L. Györffy, D. D. Johnson, and F. J. Pinski, J. Phys. F: Met. Phys. **18**, 719 (1988).

[39] D. E. Ellis and G. S. Painter, Phys. Rev. B **2**, 2887 (1970).

[40] D. E. Ellis and D. Guenzburger, Adv. Quantum Chem. **34**, 51 (1999), and references therein.

[41] D. Guenzburger and D. E. Ellis, Phys. Rev. B **51**, 12519 (1995).

[42] D. Guenzburger and D. E. Ellis, Phys. Rev. B **52**, 13390 (1995).

[43] D. Guenzburger and D. E. Ellis, Phys. Rev. B **49**, 6004 (1994).

[44] D. Guenzburger and D. E. Ellis, Phys. Rev. B **45**, 285 (1992).

[45] D. Guenzburger and D. E. Ellis, Phys. Rev. Lett. **67**, 3832 (1991).

[46] J. A. Gómez and D. Guenzburger, Phys. Rev. B **63**, 134404 (2001).

[47] J. A. Gómez and D. Guenzburger, J. Phys.: Condens. Matter **14**, 12311 (2002).

[48] J. Terra and D. E. Ellis, Phys. Rev. B **56**, 1834 (1997).

[49] J. Terra and D. Guenzburger, Phys. Rev. B **44**, 8584 (1991).

[50] S. H. Vosko, L. Wilk, and M. Nusair, Can. J. Phys. **58**, 1200 (1980).

[51] B. Delley and D. E. Ellis, J. Chem. Phys. **76**, 1949 (1982).

[52] *Mössbauer Isomer Shifts*, edited by G. K. Shenoy and F. E. Wagner (North-Holland, Amsterdam, 1978).

[53] J. Terra and D. Guenzburger, J. Phys. Chem. **99**, 4935 (1995).

[54] N. N. Greenwood and T. C. Gibb, *Mössbauer Spectroscopy* (Chapman and Hall, London, 1971).

[55] A. Abragam, *The Principles of Nuclear Magnetism* (Oxford University Press, Oxford, 1961).

[56] D. Guenzburger and D. E. Ellis, Phys. Rev. B **36**, 6971 (1987).

[57] P. Blaha, K. Schwarz, and P. H. Dederichs, Phys. Rev. B **37**, 2792 (1988).

[58] P. Dufek, P. Blaha, and K. Schwarz, Phys. Rev. Lett. **75**, 3545 (1995).

[59] G. Y. Guo and H. Ebert, Phys. Rev. B **53**, 2492 (1996).

[60] D. G. Rancourt, K. Lagarec, A. Densmore, R. A. Dunlap, J. I. Goldstein, R. J. Reisener, and R. B. Scorzelli, J. Magn. Magn. Mater. **191**, L255 (1999).

[61] E. de Grave, R. E. Vandenberghe, P. M. A. de Bakker, A. van Alboom, R. Vochten and R. van Tassel, Hyperfine Interact. **70**, 1009 (1992).

[62] C. S. Wang, B. M. Klein, and H. Krakauer, Phys. Rev. Lett. **54**, 1852 (1985).

[63] K. Knöpfle, L. M. Sandratskii, and J. Kübler, Phys. Rev. B **62**, 5564 (2000).

[64] Y. A. Abdu, T. Ericsson, H. Annersten, N. A. Dubrovinskaia, L. S. Dubrovinsky, and A. M. Gismelseed, Hyperfine Interact. **5**, 375 (2002).

[65] D. Guenzburger and D. E. Ellis, Phys. Rev. B **31**, 93 (1985), and references therein.

[66] R. Ingalls, F. van der Woude, and G. A. Sawatzky, in *Mossbauer Isomer Shifts*, edited by G. K. Shenoy and F. E. Wagner (North-Holland, Amsterdam, 1978).

[67] I. Dézsi, U. Gonser, and G. Langouche, Phys. Rev. Lett. **62**, 1659 (1989).

[68] H. Maruyama, R. Pauthenet, J. C. Picoche, and O. Yamada, J. Phys. Soc. Jpn. **55**, 3218 (1986).

[69] H. Zähres, M. Acet, W. Stamm, and E. F. Wassermann, J. Magn. Magn. Mater. **72**, 80 (1988).